arXiv:astro-ph/9712066v1 4 Dec 1997

to appear in the *Astrophysical Journal*

Hα Velocity Mapping of Ultraluminous Infrared Galaxies

J. Christopher Mihos[1,2,3]
Department of Physics and Astronomy
Johns Hopkins University, Baltimore, MD 21218
hos@burro.astr.cwru.edu

and

Gregory D. Bothun
Department of Physics
University of Oregon, Eugene, OR 97403
nuts@moo.uoregon.edu

ABSTRACT

We use imaging Fabry-Pérot observations to explore the dynamical conditions in four southern ultraluminous ($L_{IR} \gtrsim 10^{12}$ L$_\odot$) infrared galaxies. These galaxies all show morphological and kinematic features indicative of a major merger, but span a wide range of inferred dynamical ages: the youngest system is just past the first encounter, while the oldest has already merged into a single object. This diversity in dynamical states indicates that ultraluminous activity is *not* confined solely to late-stage mergers. The Hα emission is more spatially concentrated in the later stage mergers, in agreement with models which show that mergers drive gas inwards towards the nucleus, but high luminosities are achieved even in young interactions where the Hα is quite extended. Our data indicate that physical details other than the dynamical phase – such as the internal structure or gas content of the galaxies – can play a strong role in determining the luminosity evolution of merging galaxies. We also find evidence

[1]Hubble Fellow

[2]Visiting Astronomer, Cerro Tololo Inter-American Observatory. CTIO is operated by AURA, Inc. under contracts to the National Science Foundation.

[3]Current Address: Department of Astronomy, Case Western Reserve University, 10900 Euclid Ave, Cleveland, OH 44106.

for massive star-forming complexes at large radius in the tidal debris, reaffirming the notion that some dwarf galaxies may be spawned during the merger of more massive disk galaxies.

Subject headings: galaxies:active, galaxies:interactions, galaxies:kinematics and dynamics, galaxies:starburst, infrared:galaxies

1. Introduction

With bolometric luminosities rivaling those of quasars, the so-called "ultraluminous infrared galaxies" (ULIRGs) are the most luminous objects in the local universe. The basic properties of these galaxies have been reviewed by Sanders and Mirabel (1996) and their most outstanding characteristics can be summarized as follows: 1) 90% of their bolometric luminosity is emitted in the wavelength range 12-100μ; 2) with one exception, all have very high CO luminosities (see Solomon et al. 1997); 3) when imaged deep enough, all show signs of strong interactions or mergers (see Melnick and Mirabel 1990, Clements and Baker 1996; Clements etal 1996a). The phenomenological picture which emerges is that ULIRGS are the manifestation of the collision and subsequent merger of two disk systems which are rich in molecular gas. Support for this picture comes from the observed molecular gas masses of ULIRGS which are consistent with what has been measured for gas-rich luminous disk galaxies (Solomon et al. 1997), as well as the refutation of the assertion by Leech et al. (1994) that some ULIRGS were not in strongly interacting systems. Better imaging by Clements and Baker (1996), Clements etal (1996ab) and Lucas etal (1997) has shown that virtually all ULIRGS show morphological signatures of a major merger.

Behind the phenomenology, however, lies the physics which produces the very high luminosities. While the trigger for the effect may now be clear, it remains controversial if starbursts (Joseph & Wright 1985) or AGN activity (Sanders et al. 1988) are the main power source of the luminosity. Both have been invoked and there is evidence to support either case. For instance, in some ULIRGs, emission line diagnostics indicate the presence of buried AGN in their nuclei, while other systems show no such evidence (Goldader et al. 1995), even in the mid-IR where the dust obscuration is less troublesome (Lutz et al. 1996). While the infrared spectra of ULIRGs are difficult to fit with a pure starburst model (Goldader et al. 1995), it remains unclear whether this is due to the presence of an AGN or simply a consequence of extreme optical depths in ULIRGs (Lutz et al. 1996). Recent ASCA observations by Ogasaka et al. (1997) reveal that at least one ULIRG has a 2-10 keV luminosity which is similar to that observed in QSOs (e.g., 10^{44-45} ergs s^{-1}). On the

other hand, VLA observations by Crawford etal (1996) shows that the radio continuum luminosity of ULIRGs is consistent with the starburst driven correlation between FIR and radio luminosity established earlier by Helou et al. (1985).

In reality, both starburst and AGN activity may be occurring concurrently, with the detailed energy balance determined by a variety of factors and there may well be some evolutionary connection between these two states. Clearly, the very high inferred densities of molecular gas (up to 10^7 cm^{-3}, Solomon et al. 1992) can generate huge starbusts. Moreover, at these densities the disk is extremely viscous (see Bryant and Scoville 1996). which greatly facilitates the viscous transport of material onto a central engine, if one exists. Hence there maybe valid physical reasons to view ULIRGs as systems that are initially powered by starbursts and then later powered by accretion onto a central engine and in that way ULIRGs affirm the starburst-AGN connection. Support for this hypothesis also comes from the work of Chang et al. (1987) who show that the dynamical lifetime of dust and other obscuring material which is in near a luminous AGN is less than the radiating lifetime of the AGN. Hence, if AGN activity is the initial power source of the ULIRGs some fraction of them should evolve to become unobscured QSOs but still show signs of merger activity. One example of this evolution might be provided by the low redshift QSO PKS 2349-014 (Bahcall et al. 1995).

To trigger either AGN or starburst activity, some mechanism must act to transport gas down to the central regions of the ULIRGs. Galaxy interactions and mergers seem the most likely mechanism to drive these central inflows of gas and this is consistent with the phenomenological picture painted above. Dynamical modeling has demonstrated the efficacy of interactions at driving inflows (Noguchi 1991; Barnes & Hernquist 1991, 1996; Mihos et al. 1992; Hernquist & Mihos 1995; Mihos & Hernquist 1996). However, the details of this link between interactions and luminous activity are not well understood. While most ULIRGs are found in closely interacting and/or merging systems, the converse is not true – the great majority of interacting systems do not display "ultraluminous" levels of emission. Clearly a crucial element in driving central activity in ULIRGs must be the detailed dynamical conditions of the interacting galaxies. Models by Barnes & Hernquist (1996) suggest that the onset and intensity of gas inflows is linked to the geometry and impact parameter of the galactic collision, while the dynamical role of central bulges in regulating inflows was demonstrated by Mihos & Hernquist (1996). Moreover, the build-up of molecular gas to high densities may also act as an efficient damper of angular momentum of additional gas which is introduced into the central regions thereby effectively serving as a conduit to fuel an AGN.

A better understanding of the conditions necessary for spawning ultraluminous

activity can only come through studies of the dynamics of ultraluminous infrared galaxies. Unfortunately, morphology alone gives only a weak handle on the dynamical state of the system. For example, while two galaxies may appear closely interacting, they may not exhibit a strong dynamical response, depending on the encounter geometry (prograde vs. retrograde encounters), the structural properties of the galaxies, or the age of the interaction. These uncertainties make it difficult to define the true dynamical state of many luminous infrared galaxies. To better investigate the dynamical conditions in ULIRGs, we present Hα velocity maps of four southern ULIRG systems, taken with the Rutgers Imaging Fabry-Pérot spectrograph. Unlike slit spectra, imaging Fabry-Pérot data map the full two velocity field of the galaxies, and the arcsecond spatial resolution achieved in the optical betters that of HI velocity maps by an order of magnitude. Using the morphology and velocity field in conjunction with numerical modeling, it is possible to reconstruct much of the dynamical history of merging systems (e.g., Borne, Balcells, & Hoessel 1988; Stanford & Balcells 1991; Mihos et al. 1993; Hibbard & Mihos 1995; Mihos & Bothun 1997) and probe the dynamical conditions necessary for driving "ultraluminous" levels of activity.

2. Observations

Our sample of ultraluminous infrared galaxies is neither complete nor unbiased. The four objects (Table 1) were chosen to have high far-IR luminosity ($L_{IR} \gtrsim 10^{12}$ $L_{\odot}$) and extended, high surface brightness tidal features. The morphological criteria were employed to maximize the likelihood of detecting Hα in the tidal features, enabling us to map the velocity field of the systems at large radii. However, selecting on the presence of tidal debris probably biases our sample towards systems in which at least one galaxy was a somewhat prograde disk, and also towards systems which are relatively young. Tidal features are much harder to detect in retrograde mergers or in very old remnants where the tidal debris has become very diffuse.

The Hα velocity mapping described here was done using the Rutgers Imaging Fabry-Pérot on the CTIO 4-m telescope. The Fabry-Pérot etalons have a bandpass of 2.2Å FWHM, giving an instrumental velocity dispersion of $\sim$ 50 km s^{-1}. To isolate the Hα transmission order, narrow band ($\sim$ 80Å) Hα filters were used. Using the Tek 2k CCD, the pixel scale was 0.36″ pixel^{-1} and the circular field of view covered $\sim$ 1.5′ in diameter. This field of view was sufficient to encompass each system, with the exception of IRAS 19254-7245, whose long tidal tails extended off the edge of the field.

Observations of each object consist of a series of 10 minute exposures typically stepped 1Å apart. The spectral range covered depends on the velocity width of the system; details

for each object are given in Table 2. We emphasize that observing time constraints made it impractical to extend spectral coverage in order to detect broad wings that might be associated with nuclear outflow or the presence of an AGN. Data reduction consisted of flat fielding, sky subtraction, and normalization of the individual images to a common transparency (see Mihos & Bothun 1997). Because the redshift range of the sample and the radial wavelength gradient across the field of view, night OH sky lines appear on the images as diffuse rings of emission. These night sky rings are removed by masking out the object and creating a map of the median intensity as a function of radius in each image, which is then subtracted from the original. Transparency normalization was done by assuming that stars in the field have a flat spectrum over the limited spectral range scanned. Because of the small field of view, only a few stars are available for photometry in each field, making accurate normalization difficult. Typical corrections for transparency are less than 20%, with errors of 5 to 10%. Wavelength calibration was achieved through a series of neon lamp exposures taken during the night.

After the images are normalized, each pixel has a spectrum associated with it which traces out the spectral shape of the Hα emission line at each point in the galaxy. Binning the images 3x3 to improve signal, the spectra are fit to a single Voigt profile using least squares minimization. From this fitting, four parameters are extracted: the continuum level, the Hα line flux, the central velocity of the line, and the gaussian velocity dispersion. Each pixel was fit automatically, after which the individual fits were examined by eye while watching *Melrose Place*. Fits to obvious noise were deleted, and bad or missing fits to good data were improved by giving the fitter a better initial estimate of the parameters. In the final maps, typical errors on the derived velocity are $\pm$20 km s^{-1}, as long as the line profile was simple. However, some regions proved difficult to fit to a single line profile, having asymmetric lines, multiple components, or velocity widths greater than the scanned spectral range. These regions are discussed in detail in §3 below.

3. Individual Objects

3.1. IRAS 14348-1447

IRAS 14348-1447 (hereafter IR14348) is the most distant and infrared luminous of the four galaxies observed (Table 1). The optical morphology (Sanders et al. 1988; Melnick & Mirabel 1990) is that of a double nucleus system, with a bright tidal tail extending to the north and a fainter tail to the southwest. Near-IR imaging reveals two nuclei (Carico et al. 1990) with a separation of $\sim 3.5''$ (5 kpc). The nuclei have a velocity difference of $\Delta v = 150$ km s^{-1} from optical emission lines, and the nuclear spectra show indications of

AGN activity, classified alternately as LINER (Veilleux et al. 1995) or Seyfert 2 (Sanders et al. 1988; Nakajima et al. 1991). Single dish CO(1-2) measurements indicate the system contains $\sim 6 \times 10^{10}$ $M_\odot$ of molecular gas (Sanders, Scoville, & Soifer 1991).

An examination of the fitted spectra showed no complex lines; all data was reasonably well fit by a single component Voigt profile. However, the spectral range scanned was not sufficient to sample the full velocity width of the Seyfert 2 line profile in the SW nucleus. The spectral line fits here are very suspect, as there is no sampling of the continuum to fit the line. In this situation, the line fitting algorithm systematically overestimates the continuum and underestimates both the line strength and velocity dispersion. As a result, estimates of the relative Hα flux and velocity dispersion in the emission line gas are only accurate outside the active nuclear region.

Figures 1 (Plate 1) and 2 show the reduced Fabry-Pérot maps for IR14348. Due to the low flux levels in the off-Hα images, the continuum map shows little more than the two nuclei, separated by $\sim 4''$. The Hα intensity map is much more complicated, with extended, clumpy emission throughout the body of the system and in the tidal tails. Interestingly, the strongest Hα in the NE member is found offset from the NE nucleus by $2''$ away from the interacting companion. This offset is clearly visible in the both reduced maps and the raw images, and is not an artifact of the spectral fitting process. It is unclear whether this non-nuclear emission is intrinsically stronger than the nuclear emission or if the nuclear region is simply more obscured – more accurate photometry and reddening corrections are needed to resolve this issue. Regardless, it is clear that the NE member is experiencing significant non-nuclear star formation.

The Hα emission is not confined to the main body of the system, either. Several discrete clumps of Hα are found at large radius, $\sim$ 5–15$''$ (7–20 kpc) from the center of the system. These include a bright emission source $5''$ to the south, extended emission in the NE tail, and a system of four compact Hα knots in the SW tail. Using the published Hα nuclear fluxes from Veilleux et al. (1995) to obtain approximate photometric zeropoints, we can get an estimate of the Hα luminosity of these objects. The compact objects in the SW tail have Hα luminosities of $\sim 5 \times 10^{39}$ erg s^{-1} each, while the more luminous object to the south has an Hα luminosity of $\sim 2 \times 10^{40}$ erg s^{-1}. While the errorbars are large (factors of several), these Hα luminosities are similar to those of the SMC and LMC respectively (Kennicutt et al. 1995). The velocity dispersion and continuum levels in these regions are low, suggesting this is extended gas which has been compressed during the collision and is now collapsing and forming stars. These regions may represent the early stages of the formation of tidal dwarf galaxies (e.g., Zwicky 1956; Mirabel, Dottori, & Lutz 1992; Hibbard et al. 1993).

From the derived Hα velocities, we measure a velocity difference between the nuclei of $\Delta v = 125 \pm 25$ km s^{-1}, consistent with previous measurements, with the NE galaxy having a relative blueshift. The velocity map shows that the merging systems each still possess coherent rotation. Extracted one dimensional velocity cuts are shown in Figure 3. The peak-to-peak velocity width of the NE galaxy is $\Delta v \sin i \sim 200$ km s^{-1}, while that for the SW galaxy is smaller $\Delta v \sin i \sim 150$ km s^{-1}, probably due to a lower inclination (recall that the SW nucleus is actually brighter in K by 0.54 mag; Carico et al. 1990). The extracted velocity cuts both run through the bright Hα knot to the south, and it is here that the velocity field shows a large (~ 100 km s^{-1}) shift to higher velocities. How this region is dynamically linked to either or both of the galaxies in the pair is unclear, but in both velocity cuts the higher velocity Hα emission occurs after the rotation curves have flattened, suggesting it is a distinct dynamical feature and not merely an extension of the rotation curve(s).

The overall two dimensional velocity field indicates that, for the NE galaxy, the encounter is fairly prograde. In both galaxies, the far side of the disks have a radial (line-of-sight) velocity in the opposite sense from the systemic velocity of their respective companion, a classic signature of a prograde encounter. More striking evidence comes from the velocity structure of the (largely edge-on) NE tail. The short, stubby tidal features produced in retrograde encounters typically have large velocity gradients, as the material is stripped out of the disk with a velocity in the opposite sense of the rotational velocity. The velocity gradient in the NW tail (Figures 2 and 3) is quite small, inconsistent with a retrograde origin. The fact that the tails are rather short (~ 20 kpc) argues either that the collision is not *highly* prograde, that the encounter is fairly young, or that projection effects are severe.

3.2. IRAS 19254-7245 (The Superantennae)

IRAS 19254-7245 (IR19254) is composed of a pair of galaxies, separated by 10 kpc, and possesses an enormous pair of tidal tails which span 350 kpc from tip to tip (Mirabel, Lutz, & Maza 1991). The southern galaxy is a Seyfert 2 nucleus, with complex emission line velocity structure nearly 1500 km s^{-1} in width (Mirabel et al. 1991; Colina, Lipari, & Macchetto 1991). Because the nuclear emission line complex is broader in width than the spectral regions scanned by the Fabry-Pérot, no fitting could be done in regions in and immediately surrounding the nucleus; these regions have been masked out in the final maps. Throughout the rest of the system, single Voigt profile fits proved adequate to describe the observed line profiles. The reduced Fabry-Pérot maps for IR19254 are shown in Figures 1

and 4.

Unlike IR14348, the strongest Hα emission in IR19254 is located within a few kpc of the nuclear regions of the galaxies. The exceptions are several Hα knots along the tidal arm of the northern galaxy and a single bright H II complex on the south side of the southern disk. In fact, the Hα flux from this bright H II region is comparable to the Hα flux from the entire northern nucleus. From longslit spectroscopy, the Hα luminosity of the northern nucleus is 10^{-14} erg s^{-1} cm^{-2} (Colina 1997, private communication), yielding an Hα luminosity for the detached star forming knot of $L_{H\alpha} \sim 7 \times 10^{40}$ erg s^{-1}, a few times larger than that of the LMC (Kennicutt et al. 1995). HST imaging of IR19254 (Borne et al. 1997) shows a bright unresolved point source at this location; the inferred size is $\stackrel{<}{\sim}$ 200 pc. The size and luminosity of this object is similar to high surface brightness blue compact dwarf galaxies (e.g., Marlowe 1997).

Because the disks in IR19254 appear more distorted than in IR14348, rather than defining a major axis and extracting rotation curves, in Figure 5 we simply plot the velocities collapsed along the east-west direction – a position-velocity plot. Even with the morphological distortion, we see that the velocity field of the system is fairly regular, showing two rotating disks with velocity widths of $\Delta v \sin i = 400$ km s^{-1} and 600 km s^{-1} for the northern and southern galaxies, respectively. Outside the central regions the velocity dispersions are moderately low except for the region between the nuclei. While the dispersion is large in this region, there are clearly two components to the line profile (Figure 6a), suggesting that rather than true random motions, we are observing two disks overlapping in projection. Both disks are rotating in the same sense, with their northern sides receding. The northern galaxy is redshifted compared to its southern companion (by $\sim$ 200 km s^{-1}), confirming the expectation of a prograde encounter based on the presence of the immense, linear tidal tails.

Extending to the east from the brighter southern nucleus is a plume of Hα which does not correspond closely to any continuum features such as spiral arms or bright knots observed in HST imaging of IR19254 (Borne et al. 1991). The Hα line profile of this region shows a strongly asymmetric blue wing (Figure 6b), suggestive of outflowing material. The luminosity weighted mean velocity of this plume is $v = 17780$ km s^{-1}, or $v - v_{nuc} = -120$ km s^{-1}, where the nuclear velocity is defined by the NaD absorption feature[4] (Colina et al. 1991). This inferred expansion velocity is much less than that of material in the nuclear regions, which have a velocity width of $v - v_{nuc} = \pm 800$ km s^{-1}(Colina et al. 1991). At

[4]Because of the multicomponent emission line profile of the southern nucleus, defining an emission line redshift for this nucleus is problematic.

a projected distance from the nucleus of 5″ (6 kpc), the material in this extended plume must be slowing as it expands outwards, as expected in starburst wind models (e.g., Koo & McKee 1992; Heckman et al. 1996). To get a simple estimate of the expansion time of this material, we note that for a spherically symmetric expanding superbubble powered by a constant mechanical luminosity, $r/v = (7/410)t_7$ where r is the radius in kpc, v the expansion velocity in km s^{-1}, and t_7 the expansion time in 10^7 years (e.g., Heckman et al. 1996). If the plume is expanding outwards at an angle i from the line of sight, we have $t_7 = (410/7)(r_{obs}/v_{obs}) \cot i$. Our derived expansion age for this Hα plume is thus $3 \times 10^7 \cot i$ years, setting a rough timescale for the starburst activity.

Of considerable interest are the velocities of the faint knots at large radius in the tidal tails, as they reveal whether the knots are physically associated with the tails and, if so, give some constraint on the expansion velocity of the tails. Because of the limited field of view of the Fabry-Pérot on the 4-m, only the the three brightest knots in the northern tail (see Figure 1 of Mirabel et al. 1991) were observable, and of these knots only the closest had detectable Hα emission (Figure 6c). The radial (line of sight) velocity of this knot is 18030 km s^{-1}, redshifted by 100 km s^{-1} from the systemic velocity of the nuclei. This detection is clear evidence that the interaction has triggered star formation in the tidal tails 60 kpc from the merging pair. Using the observed quantities, we get an expansion age of $r_{obs}/v_{obs} = 6 \times 10^8$ years, but this again is very crude, subject to projection effects and geometry. However, a lower limit on the expansion age can be estimated from the circular velocity of the disks; dynamical models of merging galaxies show that the tail expansion velocity is not larger than the circular velocity (Hibbard & Mihos 1995; Mihos, Dubinski, & Hernquist 1997). Taking 300 km s^{-1} as an upper limit to the tail velocities, a lower limit to the expansion age is then 2×10^8 years. It is clear that the starburst age (as measured by the Hα plume expansion) is much shorter than the dynamical age of the merger (as measured by the tails). Unlike IR14348, IR19254 "waited" a few dynamical times after the initial collision before entering its ultraluminous phase.

3.3. IRAS 20551-4250

IRAS 20551-4250 (IR20551) is a single object with a relatively high surface brightness tidal tail to the south and a fainter tidal plume to the north. The surface brightness profile is reasonably well fit by an $r^{\frac{1}{4}}$ law (Johansson 1991), except for in the central regions where it flattens; this profile is typical of the mass profiles of modeled merger remnants (e.g., Barnes 1992; Hernquist 1992) where violent relaxation redistributes the stellar mass in an $r^{\frac{1}{4}}$ mass profile. The fact that we see this quasi-elliptical light profile suggests that the

violent relaxation in IR20551 is largely complete and the two nuclei have assimilated into one central mass.

The reduced Fabry-Pérot maps of IR20551 are shown in Figures 1 and 7. The continuum map shows the single body along with a bright "ridge" to the southeast – probably a tidal arm or loop similar to those seen, for example, in NGC 7252 (Schweizer 1982; Hibbard et al. 1995). The long tidal tail extending to the south is extremely diffuse, with none of the high surface brightness knots seen in IR19254 or IR14348.[5] The Hα emission is concentrated in the central regions with only weak extended emission visible. The notable exception is an Hα knot to the southeast of the nucleus, where the tidal loop meets the main body. Very faint emission is seen in the loop itself as well as in the tidal plume to the north; however, no H II regions are seen in the long southern tidal tail.

The Hα velocity field of the galaxy is very regular, and indicative of simple circular motion, with a velocity width of $\Delta v \sin i = 150$ km s^{-1}. This rotating disk of ionized gas is similar to those found in dynamical models of mergers, where gas which is not driven into the central regions settles into a warped, diffuse disk once violent relaxation has subsided (e.g., Mihos & Hernquist 1996). The low velocity width for such a luminous system suggests we are viewing this disk largely face-on. If subsequent evolution is mild, this disk may end up resembling the H I disk found in the nearby peculiar elliptical NGC 5128 (van Gorkom et al. 1990). The only region that departs from the pattern of circular motion is the region near the tidal loop where material stripped out into tidal features is expected to be moving on very non-circular orbits (e.g., Hernquist & Spergel 1992; Hibbard & Mihos 1995).

Although no H II regions are seen in the southern tidal tail, we searched for diffuse Hα by summing the pixel intensities in a 10″x10″ patch along the tail at a distance of 35″ (30 kpc) from the nucleus. Diffuse Hα is observed (Figure 8) at a velocity of 12500 km s^{-1}, blueshifted by 100 km s^{-1} from the systemic velocity of the remnant. At such diffuse levels of Hα emission, it is unclear whether the ionizing source is diffuse star formation in the tidal tail or the extragalactic UV background.

From a dynamical standpoint, IR20551 seems to be the most quiescent of the ultraluminous IR galaxies we observed. The lack of a multiple nucleus, the centrally concentrated Hα, and the regular velocity field all argue that the period of violent relaxation associated with the merging is largely over, and that subsequent dynamical evolution will be slow. Population synthesis modeling of the spectral features in the nuclear regions by Johansson (1991) also suggests that the starburst event peaked a few times 10^7 years ago. While still ultraluminous, we may be catching IR20551 just past the peak of its luminous

[5]Note that the bright compact object to the northwest is a foreground star (Johansson 1991).

phase, as violent relaxation ends and the starburst begins to fade. The coincidence between the end of violent relaxation and the possible decline in the starburst intensity suggests that ultraluminous starbursts do not continue long after the merger is complete.

3.4. IRAS 23128-5919

IRAS 23128-5919 (IR23128) is another double nucleus system, with a separation of 4″ (3.5 kpc), and possesses a pair of tidal tails spanning 50″ (45 kpc) from tip to tip. Bergval & Johansson (1985) classify the nuclear spectrum as intermediate between Seyfert 2 and LINER, and claim to detect large scale outflow signatures in the form of asymmetric emission lines and an offset between the emission and absorption line velocities of the nucleus. Johansson & Bergvall (1988) also find Wolf-Rayet features in the galaxy spectrum, indicating a strong on-going starburst. A bright compact object is found near the end of each tidal tail, suggestive again of star-forming knots; however, Bergval & Johansson (1985) were unable to detect emission from these knots.

IR23128 proved the most complex system for fitting line profiles. Emission in the tails and the northern galaxy was well fit by single Voigt profiles, but the line profiles in the southern object were very complex, showing asymmetric shapes or double-line profiles. In such cases, a single symmetric Voigt profile is a poor model for the emission line, and these fits give poor values for the derived line parameters. For this reason, we chose to model obviously distorted lines as a sum of two Voigt profiles. This choice is not meant to imply two kinematic subsystems at each spatial point, but simply to provide a better fit to the line shape (although in several regions two distinct kinematic profiles *are* indicated by the data). With this change in fitting procedure, the derived quantities take on a slightly different meaning. The meaning of the continuum map is unchanged, while the Hα intensity map is now the sum of the flux in the two fitted lines. The velocity map now expresses the intensity-weighted mean velocity in the line, and the dispersion map shows the second moment of the profile shape. The reduced Fabry-Pérot maps for IR23128 are shown in Figures 1 and 9.

The continuum map shows the double nucleus and, faintly, the tidal tails stretching north-south. Near the end of the tails, the compact objects are easily visible. The southern galaxy is extended east-west; we argue below that this structure is a rotating disk-like component, perhaps the original disk of the southern galaxy. In the Hα map, both nuclei show strong emission, along with strong Hα between the two nuclei. Coincident with the east-west extension of the continuum light, the Hα traces out a flattened disk with strong spiral features around the southern nucleus. Several H II regions are found in the tidal

tails. Interestingly, the strongest Hα peaks in the tails do not correspond to the compact continuum sources. No emission is detected from the continuum source in the northern tail, while the southern object sits on the secondary Hα peak in that tail. The strongest Hα peaks in the tails do not have detectable continuum emission. This lack of a strong correlation between continuum peaks and Hα peaks suggests that the formation of tidal dwarfs is a stochastic process; continuum knots may be more evolved versions of Hα knots, so that at any given time a spread in population ages is observed. If so, this may make it difficult to finely date the ages of merger remnants through the stellar populations in tidal dwarfs and globular clusters (e.g., Zepf et al. 1995; Schweizer et al. 1996).

The Hα velocity map reveals a rather chaotic velocity field; Figure 10 shows the projected position-velocity plot. The tidal tails are moving in opposite directions with a velocity spread of $\pm$100 km s^{-1}. The velocity gradients along the tails are smooth, and indicate an axis of rotation along a position angle of 90°. In the southern galaxy we find clear rotation, with a velocity spread of 400 km s^{-1}. The morphology and large velocity spread in this component suggests we are seeing it nearly edge on and that it is rotating about an axis of position angle $\sim$ 0°. Rotation in the northern galaxy is less clear, although there is some hint in the position-velocity plot that there is a weak retrograde sense to its motion. The fact that this signature is weak, if present at all, indicates that we see this system largely face-on. In the region between the nuclei the velocity patterns shift again; here the lines are broad and asymmetric, so it is difficult to determine whether this is another shift in the net rotation axis or simply material decoupling from the overall rotation pattern due to collisional shocks or winds.

The second moment ("dispersion") map shows the largest velocity widths occur along the edge of the rotating disk, away from the galactic nuclei. It is here that we see broad lines which often are broken up into two distinct components (Figure 11). Much of the broadening of the line profiles must be due to the fact that we are viewing multiple kinematic components along the same line of sight. It is thus difficult to unambiguously determine the presence of galactic wind in IR23128. The nuclear spectra on which Bergvall & Johansson (1985) based their wind detection had 6Å resolution and was taken through a $4''$x$2''$ aperture centered on the nuclei – this aperture contains a significant amount of flux from the blueshifted portion of the rotating disk, which may explain most, if not all, of the blue wing seen in their low resolution spectra. To be sure, we also observe spectra with strong blue wings, but these are in regions near the disk component and may simply be due to line blending rather than true outflowing winds. Higher spectral resolution is necessary to resolve this issue.

The question of galactic winds aside, it is clear the dynamical state of IR23128 is

very complex. The axis of rotation shifts by 90° between the outer tidal features and the rotating southern disk, while the northern galaxy shows a somewhat retrograde motions, around a rotation axis orthogonal to that of the southern disk. The tidal features generally trace much of the initial angular momentum of the system; the fact that the inner disk has been slewed by 90° suggests that the gravitational torques have been strong and slow, i.e. that IR23128 is well past the first encounter and now experiencing the final destructive merging phase. The multiple kinematic components within the merging pair cannot survive for long – collisional shocks and gravitational torques will rapidly erase these features and drive strong inflow (e.g., Mihos & Hernquist 1996). We are most likely witnessing IR23128 in a very shortlived phase where violent relaxation is rapidly altering the structural and dynamical properties of the system.

4. Discussion

Although our sample of ultraluminous IRAS galaxies is necessarily small, we nevertheless have detected a wide variety of dynamical states, even though the bolometric luminosities are all quite similar. The combined morphological and kinematic features in the galaxies suggests the following age-ordering for the four systems:

- IR14348 is the dynamically youngest as indicated by its short tidal tails, relatively unperturbed kinematics, and widely distributed star formation. The system has not merged yet and its first dynamical response to the initial encounter is the initiation of wide spread star formation, which likely powers much of the observed IR luminosity. Strong gaseous inflows may not yet have developed in IR14348, and this system may be analogous to other "young" ultraluminous systems such as II Zw 96, VV 114, and Arp 299 (e.g., Yun, Scoville, & Knop 1994; Goldader et al. 1997).

- IR19254 is well past the first collision as evidenced by the long tidal tails. The two disks are still well-separated ($\sim$ 10 kpc) and their coherent rotation suggest it is not yet in the latest stages of merging. It is unclear if the Seyfert activity in the southern galaxy is a response to the current interaction or was a pre-existing condition. The strong Hα seen near the nuclear regions suggests the interaction is sufficiently advanced that gas is starting to flow inwards.

- IR23128 is dynamically complex. It is currently experiencing strong dynamical perturbation. This coupled with its close projected separation and distorted kinematics indicate it is the final merging phase and most of the emission is concentrated in the central regions. Some evidence for kinematic feedback and

baryonic blow out of the nuclear gas exists and this system may therefore be in a similar state as Arp 220 (e.g., Heckman etal 1996).

- IR20551 has a single nucleus and a quiescent velocity field. These are the conditions expected in the post-merger phase of the interaction where only its remnant tidal features attest to a merger origin for the system. Star formation is no longer widespread in the system and its likely that its ultraluminous phase is near the end.

Given this putative dynamical age dating sequence, it is somewhat surprising that at similar bolometric luminosity we see such a range of dynamical conditions. Our sample was chosen to have high infrared luminosity, and one might have expected that this criteria would have strongly biased our sample towards late stage mergers. While the sample is small, we do not see any strong bias. We do see a trend between dynamical age and Hα concentration, in that more evolved systems seem to have more centrally concentrated Hα emission (due to central starbursts or AGN). This is consistent with the idea that collisions drive disk gas into the nucleus over a few dynamical times during the encounter. Nonetheless, it is somewhat surprising that such high luminosities can be achieved in young objects with extended emission as well as the more evolved, concentrated objects. Clearly, ultraluminous activity is not confined solely to late stage mergers where the gaseous inflows are complete.

At face value, the fact that these ultraluminous infrared galaxies are found in a variety of dynamical phases might indicate that the ultraluminous phase is long-lived. If the observed luminosity is powered by star formation, this would require starburst activity to last several dynamical timescales. Such a scenario is rather difficult to envision. Spectral modeling of ultraluminous starbursts by Goldader et al. (1997) indicate starburst lifetimes of $\sim 10^8$ years, much less than typical merging times of $\sim 5 \times 10^8$ years. Furthermore, for inferred star formation rates of 100 $M_\odot$ yr^{-1} (e.g., Leitherer & Heckman 1995; Goldader et al. 1997), the gas depletion times are $\sim 5 \times 10^7$ years, again much shorter than the merging timescale; truncating the IMF below 1 $M_\odot$ increases the depletion times by only a factor of two (Goldader et al.). It would thus seem unlikely that sustained ultraluminous starburst activity is possible in these systems. Perhaps a more stochastic starburst model, where a series of mini-bursts with a long "duty cycle" occurs over a few dynamical timescales, might supply the observed luminosity, although such a scenario seems rather contrived.

An alternative would be to appeal to AGN activity as the primary source of the luminosity. In this case the timescale mismatch is significantly lessened as sufficient gas is available to sustain AGN activity over a few dynamical timescales. However, the relatively

long time spent by interacting galaxies at apogalacticon would result in a large fraction of ultraluminous IRAS galaxies being observed in wide pairs if the ultraluminous phase does span the merging timescale. This prediction is in the opposite sense of the observed morphological trends (Murphy et al. 1996), where most ultraluminous systems are found to be close mergers.

Given that a long-lived ultraluminous phase is inconsistent both with observational data and physical considerations, we are driven by our data to the more likely view that dynamical phase is not the single triggering criteria for ultraluminous activity. A variety of other factors must therefore contribute to the formation of ultraluminous infrared galaxies. While the merger mechanism is the root cause of the observed activity, important physical details likely determine the particular luminosity evolution of a given system. Some of these other factors include 1) the orbital geometry of the encounter (e.g., Barnes & Hernquist 1996), 2) the internal structure of the merging galaxies (Mihos & Hernquist 1994, 1996), or 3) the total amount of gas in the pre-merger disks. Our small data sample does not permit definitive conclusions but an important clue comes from the fact that we are witnessing ultraluminous activity in two galaxies which have yet to experience the violent relaxation associated with the merger (IR14348 and IR19254), arguing that internal processes play an important role in determining the response of galaxies to the encounter. Both of these encounters are clearly prograde, as evidenced by the long tidal tails and velocity field in IR19254 or the velocity field of IR14348. IR14348 is probably just past the first collision and significantly dynamically younger than the other three systems. Dynamical models show that the strongest inflows (and, presumably, starbursts) occur during the final merging, and are concentrated in the nuclear regions of the system (Barnes & Hernquist 1991, 1996; Mihos & Hernquist 1994, 1996). While IR19254, IR20551, and IR23128 fit this general pattern, why did IR14348 become ultraluminous at an earlier phase, with star formation over a much larger spatial extent?

The answer may lie in the ambient properties of the disks. IR14348 is has the highest molecular gas mass of any of the objects in our sample with an inferred molecular mass $\sim 6 \times 10^{10}$ $M_{\odot}$ – two to three times that of the other objects (Mirabel et al. 1990; Sanders et al. 1991). With such a large reservoir of gas, the perturbation at first encounter may drive gas into collapse *locally*, increasing gas densities and boosting star formation throughout the system without needing to wait for global instabilities to drive gas inwards and fuel a central starburst. As the system evolves, central gas flows will fuel a central starburst thus changing the relative contributions of nuclear vs extended star formation to the total emitted energy. Indeed, it is interesting to note that the star forming morphology of this system is similar to the morphology of high redshift galaxies in the Hubble Deep Field (e.g., Abraham et al. 1996; van den Bergh et al. 1996; Giavalisco et al. 1996); IR14348 may

represent a low redshift analogue of gas-rich star forming galaxies in the early universe.

In our sample of ultraluminous infrared galaxies, we also find several examples of extremely luminous Hα knots in tidal tails. These knots have Hα luminosities comparable to that of the Large and Small Magellenic Clouds, and their relatively low velocity dispersions suggest they are pockets of gas in isolated collapse; if they have sufficient mass to resist baryonic blowout, they may well evolve into bona-fide dwarf galaxies (Zwicky 1956; Duc & Mirabel 1994; Barnes & Hernquist 1992). These objects seem to be more common in the less evolved systems IR14348 and IR19254; by later stages of the merging evolution they may have depleted their gas and ceased star formation or, in instances where these clumps form close to their host galaxies, fallen back into the merger remnant. At the very least, however, our data clearly shows that objects like dwarf galaxies can form in the early stages of a merger encounter at distances up to 50 kpc away from the main merging bodies.

In summary, the velocity fields of ultraluminous infrared galaxies prove quite diverse. There does not appear to be a common dynamical feature among all four objects, other than the simple fact that they are all strongly interacting. The variety of ages and kinematic features suggest that several different factors play a role into triggering ultraluminous activity, including interaction geometry, galactic structure, and gas content. While numerical models do a reasonable job of describing the evolution of galaxy mergers in a statistical sense, one-to-one matching of individual systems will prove more problematic due to varying initial conditions for different interacting pairs. From a galaxy evolution standpoint, our data reveal the strong and rapid dynamical evolution associated with violent relaxation in the final merging phase. The two objects which have not yet experienced this final phase – IR14348 and IR19254 – are comprised of relatively simple rotating disks. On the other hand, IR20551 is perhaps only a few$\times 10^7$ years past its merger, yet it already has settled down into a quiescent kinematic phase. Only IR23128 shows the very disturbed kinematics expected as two galaxies ultimately merge, and the lifetime for this phase must be short. Over the long dynamical history of a merger event, it is only in the final phase that strong dynamical evolution occurs on global scales. Once the merger is complete and the starburst quickly fades, the remnant will evolve rather quiescently; however, signatures of the merger remain behind – diffuse gas disks, tidal features, and, possibly, young dwarf galaxies – which attest to this violent phase of galaxy evolution.

We thank Ted Williams for observing support during the run, and Charles Beauvais for helpful discussions during data reduction. JCM is supported by NASA through a Hubble Fellowship grant # HF-01074.01-94A awarded by the Space Telescope Science Institute, which is operated by the Association of University for Research in Astronomy, Inc., for NASA under contract NAS 5-26555.

REFERENCES

Abraham, R.G. et al. 1996, MNRAS, 279, L47

Bahcall, J.N., Kirhakos, S., & Schneider, D.P. 1995, ApJ, 454, L175

Barnes, J.E. 1992, ApJ, 393, 484

Barnes, J.E., & Hernquist, L. 1991, ApJ, 370, L65

Barnes, J.E., & Hernquist, L. 1992, Nature, 360, 715

Barnes, J.E., & Hernquist, L.1996, ApJ, 471, 115

Borne, K.D., Balcells, M., & Hoessel, J.G. 1988, ApJ, 333, 567

Borne, K.D., Bushouse, H., Colina, L., & Lucas, R.A. 1997, in preparation

Bryant, P.M., & Scoville, N.Z. 1996, ApJ, 457, 678

Carico, D.P. et al. 1990, ApJ, 349, L39

Chang, C.A., Schiano, A.V.R., & Wolfe, A.M. 1987, ApJ, 322, 180

Clements, D.L., & Baker, A.C., 1996, A&A, 314, L5

Clements, D.L., Sutherland, W.J., McMahon, R.G., & Saunders, W. 1996, MNRAS, 279, 477

Colina, L., Lipari, S., & Macchetto, F. 1991, ApJ, 379, 113

Crawford, T., Marr, J., Partridge, B., & Strauss, M.A. 1996, ApJ, 460, 225

Duc, P.-A., & Mirabel, I.F. 1994, A&A, 289, 83

Giavalisco, M., Livio, M., Bohlin, R.C., Macchetto, F.D., & Stecher, T.P. 1996, AJ, 112, 369

Goldader, J.D., Goldader, D.L., Joseph, R.D., Doyon, R., & Sanders, D.B. 1997, preprint

Goldader, J.D., Joseph, R.D., Doyon, R., & Sanders, D.B. 1995, ApJ, 444, 97

Goldader, J.D., Joseph, R.D., Doyon, R., & Sanders, D.B. 1997, ApJ, 474, 104

Heckman, T.M., Dahlem, M., Eales, S.E., Fabbiano, G., & Weaver, K. 1996, ApJ, 457, 616

Helou, G., Soifer, B.T., & Rowan-Robinson, M. 1985, ApJ, 298, L7

Hernquist, L. 1992, ApJ, 400, 460

Hernquist, L., & Mihos, J.C. 1995, ApJ, 448, 41

Hernquist, L., & Spergel, D.N. 1992, ApJ, 399, L117

Hibbard, J.E., Guhathakurta, P., van Gorkom, J.H., & Schweizer, F. 1994, AJ, 107, 67

Hibbard, J.E., & Mihos, J.C. 1995, AJ, 110, 140

Joseph, R.D., & Wright, G.S. 1985, MNRAS, 214, 87

Johansson, L. 1991, A&A, 241, 389

Kennicutt, R.C., Bresolin, F., Bomans, D.J., Bothun, G.D., & Thompson, I.B. 1995, AJ, 109, 594

Kim, D.-C., Sanders, D.B., Veilleux, S., Mazarella, J.M., & Soifer, B.T. 1995, ApJS, 98, 129

Koo, B.-C., & McKee, C.F. 1992, ApJ, 388, 103

Leech, K.J., Rowan-Robinson, M., Lawrence, A., & Hughes, J.D. 1994, MNRAS, 267, 253

Leitherer, C., & Heckman, T.M. 1995, ApJS, 96, 9

Lutz, D. et al. 1996, A&A, 315, L137

Marlowe, A.M. 1997, Ph.D. thesis, Johns Hopkins University

Melnick, J., & Mirabel, I.F. 1990, A&A, 231, L19

Mirabel, I.F., Booth, R.S., Garay, G., Johansson, L.E.B., & Sanders, D.B. 1990, A&A, 236, 327

Mirabel, I.F., Dottori, H., & Lutz, D. 1992, A&A, 256, L19

Mirabel, I.F., Lutz, D., & Maza, J. 1991, A&A, 243, 367

Mihos, J.C., & Bothun, G.D. 1997, ApJ, 481, 741

Mihos, J.C., Bothun, G.D., & Richstone, D.O. 1993, ApJ, 418, 82

Mihos, J.C., Dubinski, J., & Hernquist, L. 1997, ApJ, in press

Mihos, J.C., & Hernquist, L. 1996, ApJ, 464, 641

Mihos, J.C., Richstone, D.O., & Bothun, G.D. 1992, ApJ, 400, 153

Murphy, T. et al. 1996, AJ, 111, 1025

Nakajima, T., Kawara, K., Nishida, M., & Gregory, B. 1991, ApJ, 373, 452

Noguchi, M. 1991, MNRAS, 251, 360

Ogasaka, Y. et al. 1997, PASJ, 49, 179

Sanders, D.B., Scoville, N.Z., & Soifer, B.T. 1991, ApJ, 370, 158

Sanders, D.B., Soifer, B.T., Elias, J.H., Madore, B.F., Matthews, K., Neugebauer, G., & Scoville, N.Z. 1988, ApJ, 325, 74

Schweizer, F. 1982, ApJ, 252, 455

Schweizer, F., Miller, B.W., Whitmore, B.C., & Fall, S.M. 1996, AJ, 112, 1839

Solomon, P.M., Downes, D., & Radford, S.J.E. 1992, ApJ, 387, L55

Solomon, P.M., Downes, D., Radford, S.J.E., & Barrett, J.W. 1997, ApJ, 478, 144

Stanford, S.A., & Balcells, M. 1991, ApJ, 370, 118

van den Bergh, S. et al. 1996, AJ, 112, 359

van Gorkom, J.H., van der Hulst, J.M., Haschick, A.D., & Tubbs, A.D. 1990, AJ, 99, 1781

Veilleux, S., Kim, D.-C., Sanders, D.B., Mazarella, J.M., & Soifer, B.T. 1995, ApJS, 98, 171

Yun, M.S., Scoville, N.Z., & Knop, R.A. 1994, ApJ, 430, 109

Zepf, S.E., Carter, D., Sharples, R.M., & Ashman, K. 1995, ApJ, 445, L19

Zwicky, F. 1956, Ergebnisse der Exakten Naturwissenschaften, 29, 344

This preprint was prepared with the AAS LaTeX macros v4.0.

Table 1: ULIRG Sample

Galaxy	Redshift (z)	Recession Velocity[a] (km s^{-1})	Distance[b] (Mpc)	d(1″)[c] (kpc)	L_{IR}[d] ($10^{12} L_{\odot}$)
IRAS 14348-1447	0.082	23715	310	1.4	1.8
IRAS 19254-7245	0.062	17910	236	1.1	1.1
IRAS 20551-4250	0.043	12660	167	0.8	1.0
IRAS 23128-5919	0.045	13100	173	0.8	0.9

[a] $V_r = c \times \sqrt{((1+z)^2-1)/((1+z)^2+1)}$.

[b] for $H_0 = 75$ km s^{-1} Mpc^{-1}, $q_0 = 1/2$.

[c] physical scale of 1″.

[d] L_{IR}=L(8-1000μm), see Sanders & Mirabel 1997).

Table 2: Observational Details

Galaxy	Wavelength Range Observed (Å)	Number of Images	Velocity Coverage (km s^{-1})
IRAS 14348-1447	7098 – 7115	18	775
IRAS 19254-7245	6954 – 6984	23	1375
IRAS 20551-4250	6838 – 6850	11	550
IRAS 23128-5919	6842 – 6868	24	1200

Color figure available at http://burro.astr.cwru.edu/preprints/ulirgs.html

Fig. 1.— Reduced Fabry-Pérot maps of all four ultraluminous systems observed. Top left: IRAS 14348-1447; top right IRAS 19254-7245 (The Superantennae); bottom left: IRAS 20551-4250; bottom right: IRAS 23128-5919. Each dataset shows the continuum map, the Hα emission map, the velocity map, and the velocity dispersion map.

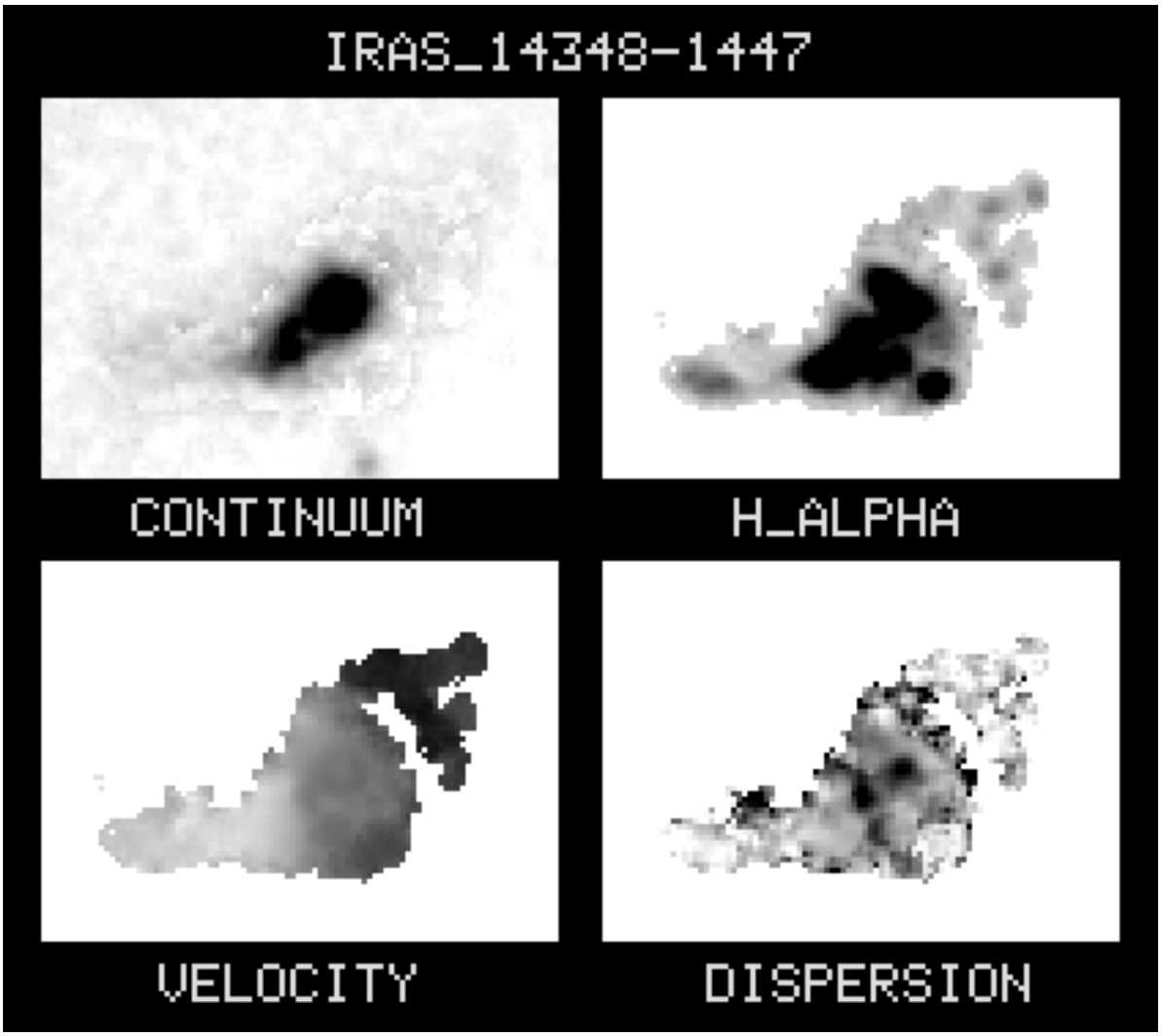

Fig. 2.— Reduced Fabry-Pérot map of IRAS 14348-1447. North is to the left; east is to the bottom. Top left: Continuum map. Top right: Hα emission map. Bottom left: Hα velocity map. Light shading is blue shifted relative to systemic; dark shading is redshifted. Bottom right: Hα velocity dispersion map. Dark regions represent high velocity dispersion.

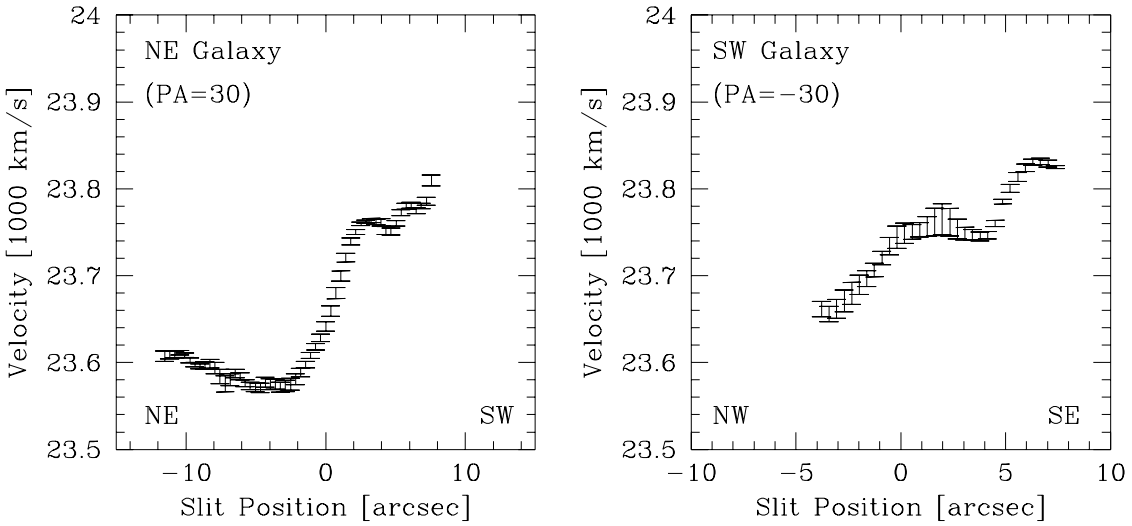

Fig. 3.— Velocity cuts through the IRAS 14348-1447 system. Left: Velocity cut through the NW galaxy at PA=30°. Right: Velocity cut through the SW galaxy at PA=−30°.

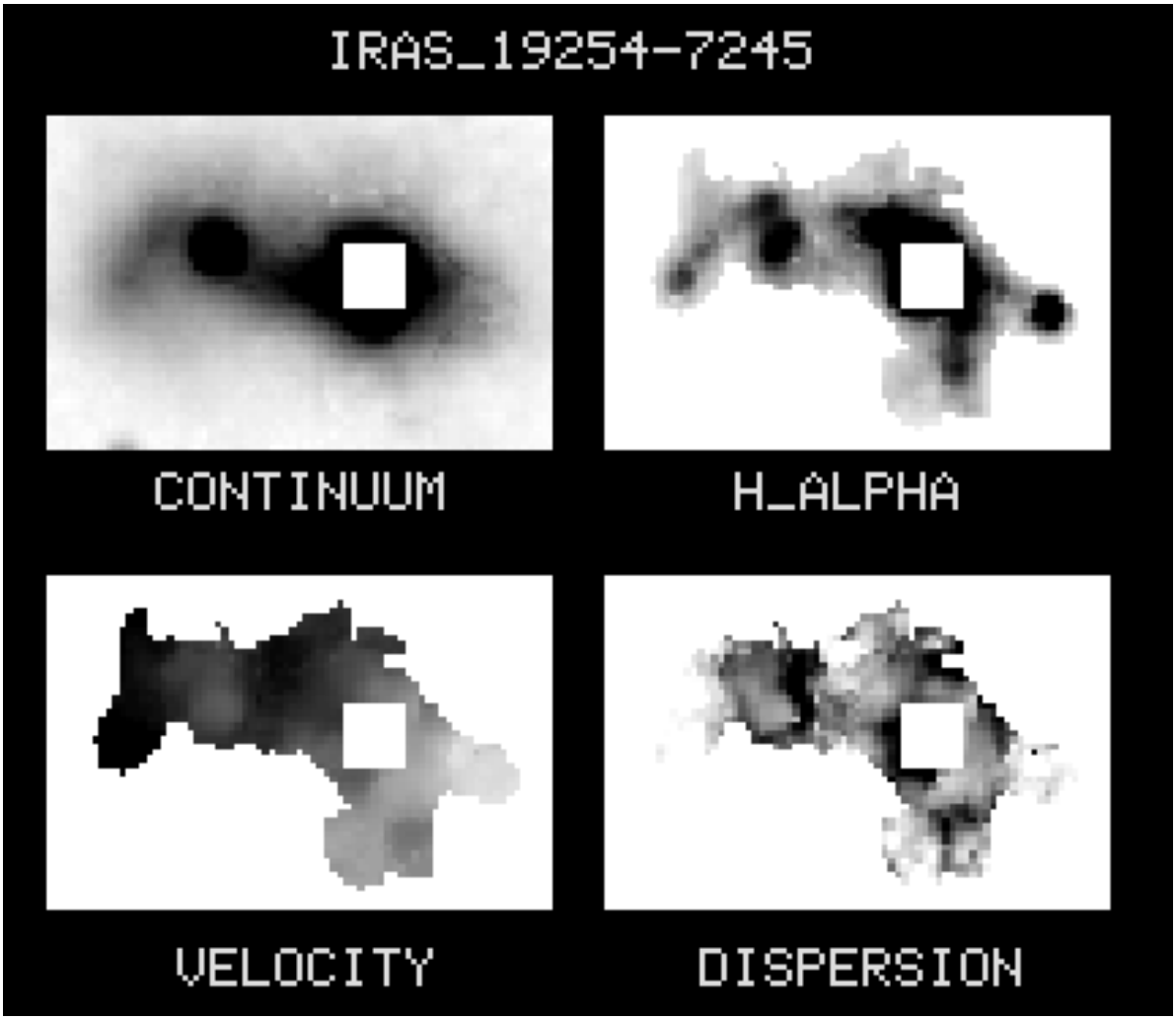

Fig. 4.— Reduced Fabry-Pérot map of IRAS 19254-7245. North is to the left; east is to the bottom. Top left: Continuum map. Top right: Hα emission map. Bottom left: Hα velocity map. Light shading is blue shifted relative to systemic; dark shading is redshifted. Bottom right: Hα velocity dispersion map. Dark regions represent high velocity dispersion. The central "hole" in the maps corresponds to the Seyfert 2 nuclear region which could not be fitted by the line fitting algorithm.

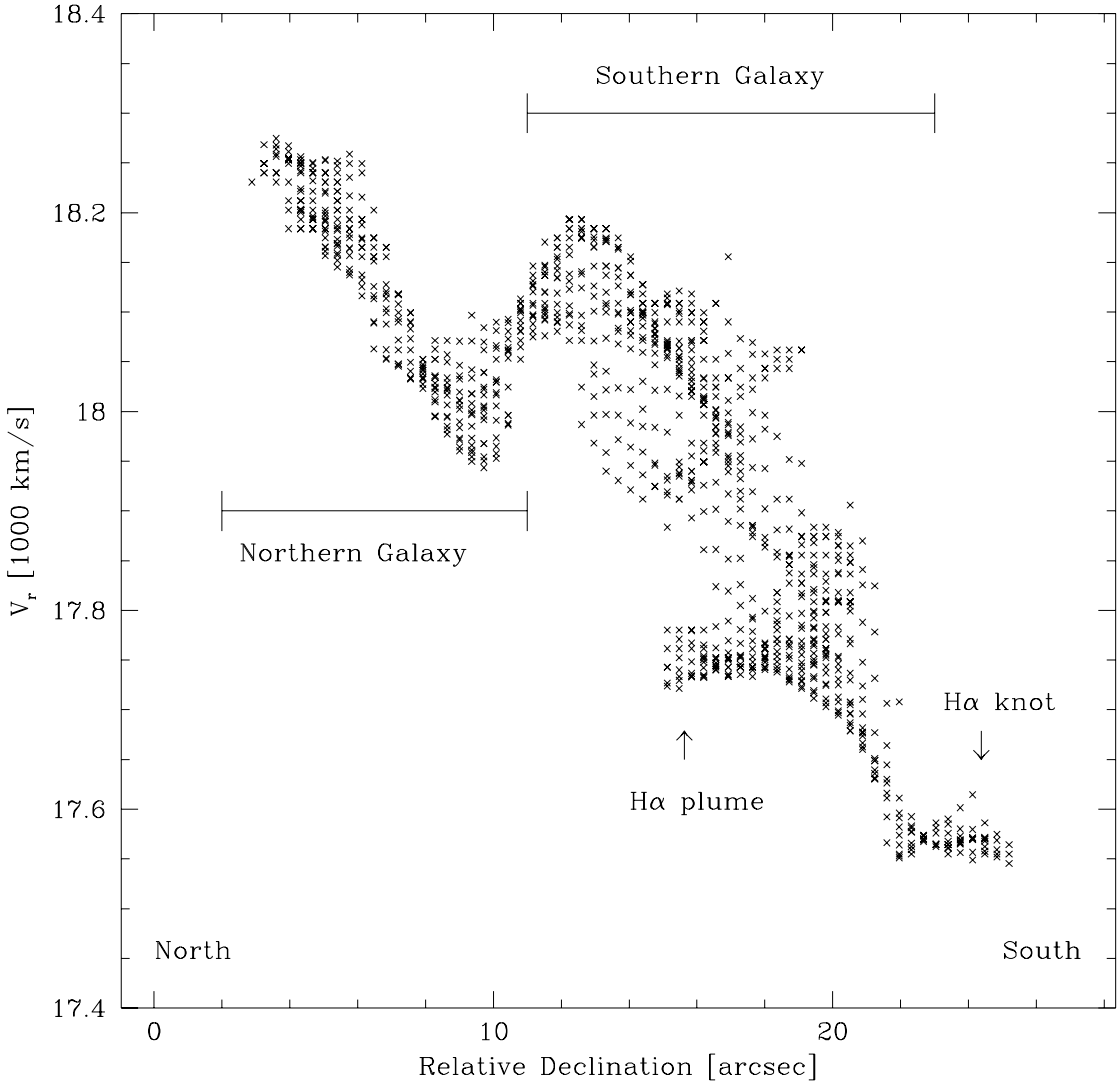

Fig. 5.— Position-velocity plot for IRAS 19254-7245. In this plot, the 2-dimensional velocity map has been collapsed in right ascension, yielding velocity as a function of declination. Two rotating disks can be seen, along with a kinematically distinct Hα plume in the southern galaxy. Note that where the two disks overlap, the velocities represent some average velocity of the distinct disk kinematics (see Figure 6).

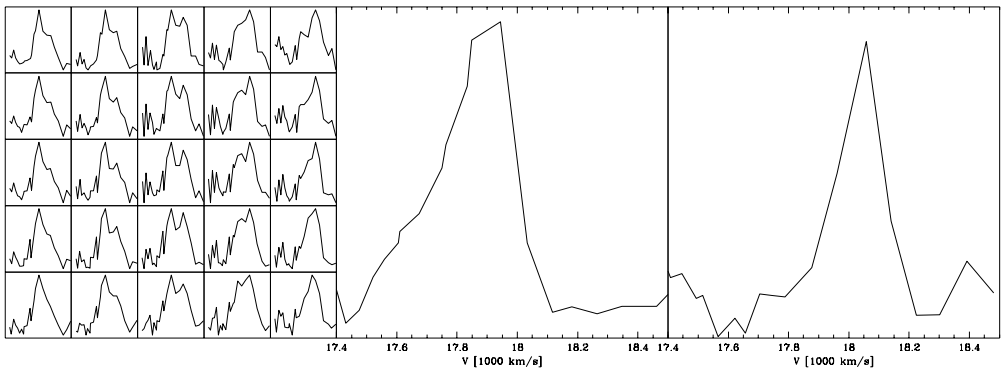

Fig. 6.— Hα emission line profiles in selected regions of IR 19254-7245. Left: The region between the two nuclei; notice the double line profile indicative of two distinct kinematic features. Middle: The Hα plume east of the southern Seyfert 2 nucleus. Right: The H II region in the northern tidal tail.

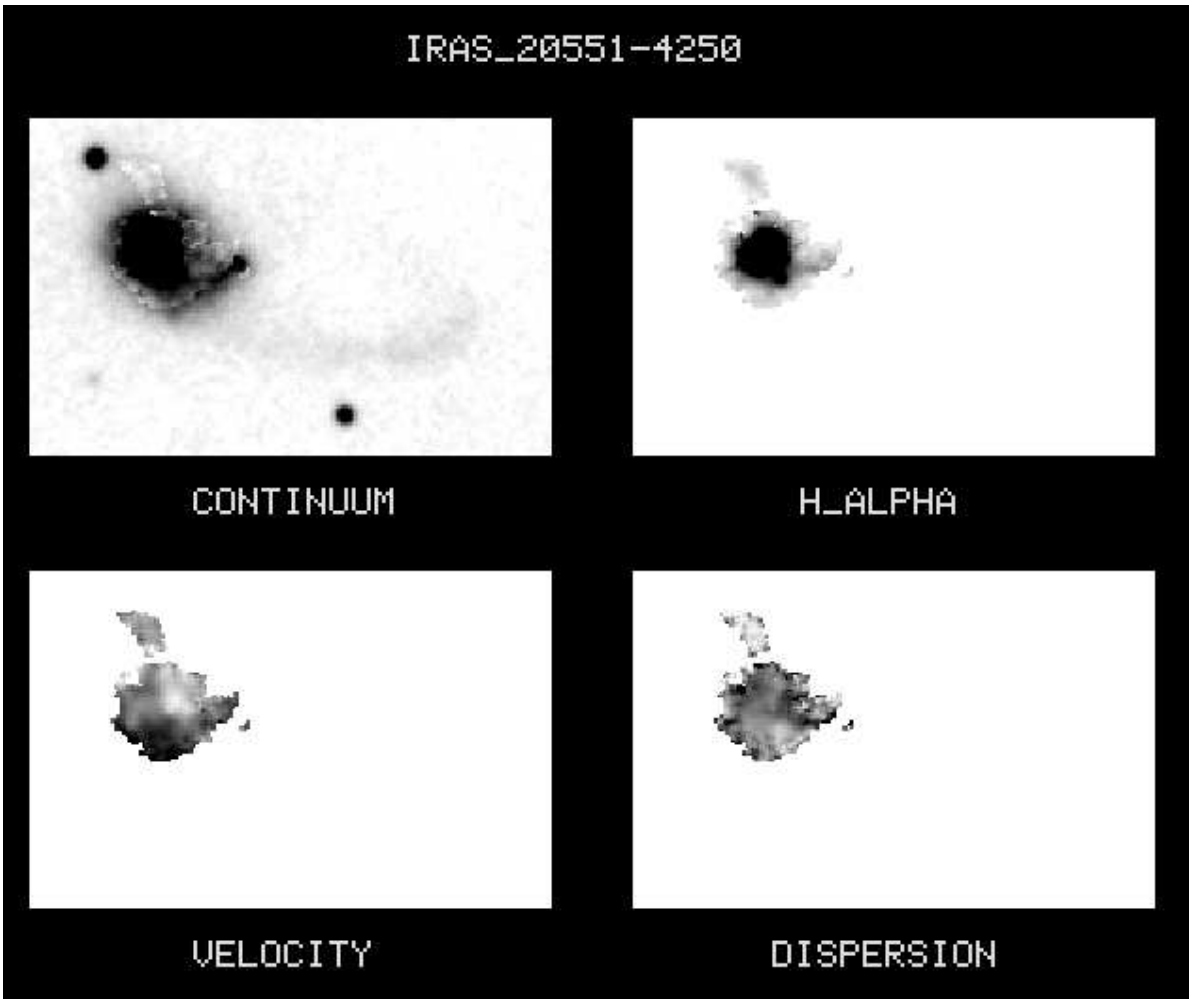

Fig. 7.— Reduced Fabry-Pérot map of IRAS 20551-4250. North is to the left; east is to the bottom. Top left: Continuum map. Top right: Hα emission map. Bottom left: Hα velocity map. Light shading is blue shifted relative to systemic; dark shading is redshifted. Bottom right: Hα velocity dispersion map. Dark regions represent high velocity dispersion.

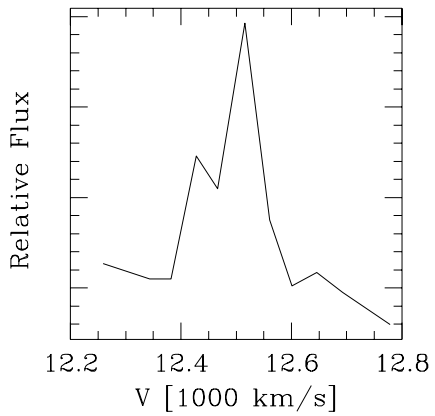

Fig. 8.— The line profile of the diffuse Hα in the southern tail of IRAS 20551-4250.

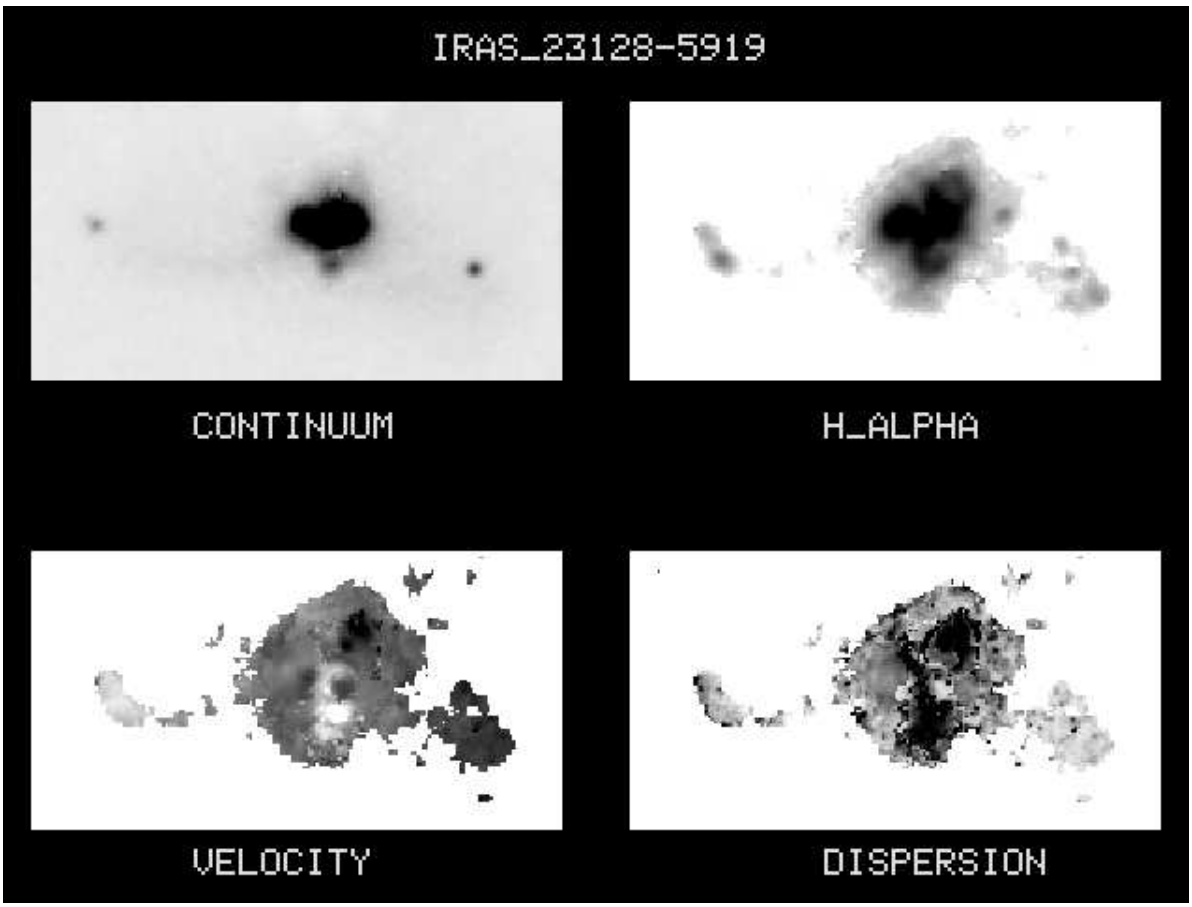

Fig. 9.— Reduced Fabry-Pérot map of IRAS 23128-5919. North is to the left; east is to the bottom. Top left: Continuum map. Top right: Hα emission map. Bottom left: Hα velocity map. Light shading is blue shifted relative to systemic; dark shading is redshifted. Bottom right: Hα velocity dispersion map. Dark regions represent high velocity dispersion.

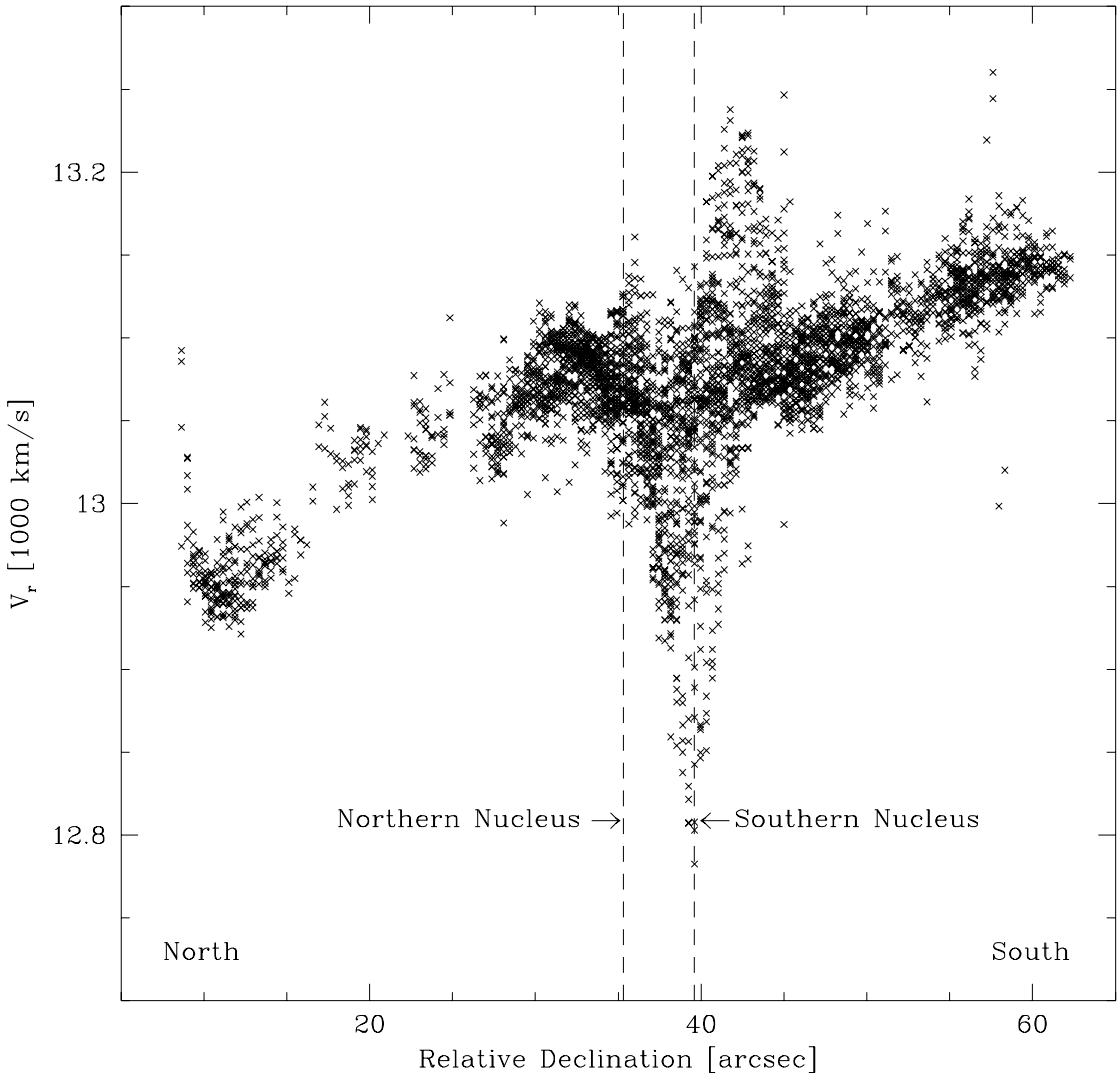

Fig. 10.— Position-velocity plot for IRAS 23128-5919. In this plot, the 2-dimensional velocity map has been collapsed in right ascension, yielding velocity as a function of declination. The dashed lines show the position of the two nuclei. A rotating component is clearly seen in the southern galaxy, and there is a weak signature of retrograde motion in the northern galaxy. The velocity gradients in the tails are also well-mapped.

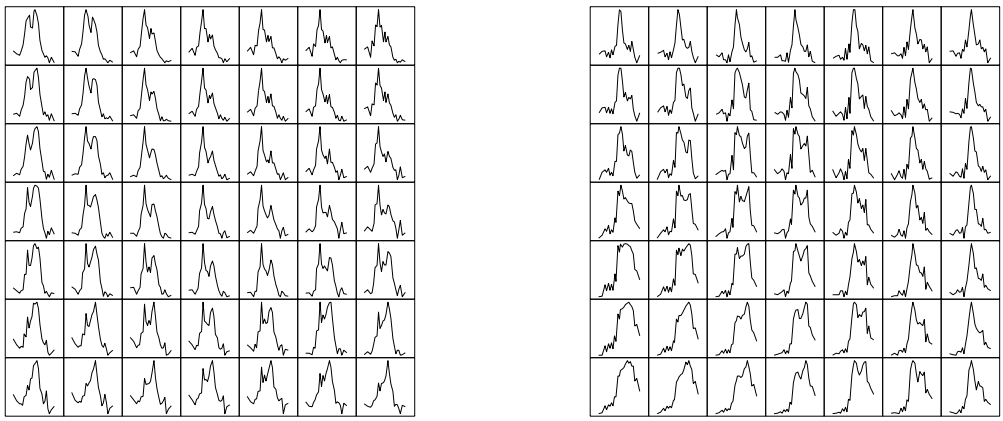

Fig. 11.— Selected line profiles in IRAS 23128-5919. Left: Profiles in the eastern, blueshifted portion of the southern disk. Right: Profiles in the western, redshifted portion of the southern disk. Note the distinct kinematic components in the spectra which shift in velocity.

This figure "f01.gif" is available in "gif" format from:

http://arXiv.org/ps/astro-ph/9712066v1